Applied Catalysis B: Environmental 294 (2021) 120257

Contents lists available at ScienceDirect

Applied Catalysis B: Environmental

journal homepage: www.elsevier.com/locate/apcatb

Advantageous roles of phosphate decorated octahedral CeO_2 {111}/g-C_3N_4 in boosting photocatalytic CO_2 reduction: Charge transfer bridge and Lewis basic site

Wanqin Li [a], Li Jin [b], Fei Gao [a,b,c], Haiqin Wan [a,c], Yu Pu [b], Xiaoqian Wei [b], Chong Chen [a], Weixin Zou [a,b,c,*], Chengzhang Zhu [a,d], Lin Dong [a,b,c,*]

[a] State Key Laboratory of Pollution Control and Resource Reuse, School of the Environmental, Nanjing University, Nanjing, 210023, PR China
[b] Key Laboratory of Mesoscopic Chemistry of MOE, School of Chemistry and Chemical Engineering, Nanjing University, Nanjing, 210023, PR China
[c] Jiangsu Key Laboratory of Vehicle Emissions Control, Center of Modern Analysis, Nanjing University, Nanjing, 210093, PR China
[d] School of Environmental and Chemical Engineering, Jiangsu University of Science and Technology, Zhenjiang, 212100, PR China

ARTICLE INFO

Keywords:
Phosphate modification
CeO_2/g-C_3N_4
CO_2 photoreduction
Charge-transfer channel
Lewis basicity

ABSTRACT

For photocatalytic CO_2 reduction, directional charge-transfer channel and abundant active sites are of significance. Herein, we designed and fabricated phosphate modified octahedral CeO_2 {111} surface coupling with g-C_3N_4 (P-CeO_2/g-C_3N_4) for photocatalytic CO_2 reduction, which had superior activity than others, i.e., P-CeO_2, g-C_3N_4, CeO_2/g-C_3N_4. The characterization results revealed the coordination environment of P species, as well as, the presence of hydrogen bond between phosphate and amino. Through the PO_4^{3-} bridge, the interfacial electrons donated from g-C_3N_4 to CeO_2, leading to the Z-scheme formation and fast photo-generated charge transfer. Furthermore, PO_4^{3-} modification increased more oxygen-containing functional groups on surface, which acted as Lewis basic sites for CO_2 reactant adsorption and activation. Therefore, under the synergistic interaction of charge-transfer channel and abundant active sites, P-CeO_2/g-C_3N_4 is a potential photocatalyst for CO_2 reduction.

1. Introduction

Carbon dioxide (CO_2) is one of the major factors contributing to the greenhouse effect of the Earth's atmosphere, and the resulting environmental problems have had a significant impact on human health [1]. One of the most promising ways to deal with this problem is to directly convert CO_2 photocatalysis into solar energy, which not only alleviates environmental problems, but also provides high-value renewable fuels [2,3]. Among all the possible methods, the semiconductor-based carbon dioxide photoreduction technology stands out for its advantages of economy, high efficiency and renewable [4–7]. Therefore, it is of great significance to develop semiconductors with high selectivity to reduce CO_2.

So far, various semiconductors include g-C_3N_4 [8,9], $ZnIn_2S_4$ [10], TiO_2 [11–13], WO_3 [14], MOF [15], CeO_2 [16–19], CdS [20], and $SrTiO_3$ [21] have been widely used in the field of photocatalysis. In many metal oxide carriers, cerium oxide (CeO_2) has a good application prospect in photocatalytic hydrogen production and CO_2 reduction, due to its abundant oxygen vacancies, unique $4f^15d^1$ orbital and the ability of Ce^{4+}/Ce^{3+} to store and release oxygen during redox [10,22–24]. In particular, it has been reported that the physical and chemical properties are dependent to the exposed crystal planes of CeO_2 [25–27]. Due to the different exposed atoms of CeO_2 surfaces, the corresponding stabilities are varies. It was showed that the CeO_2 {111} facet was provided with the lowest surface energy, {110} facet was followed, and {100} facet had the highest surface energy [28]. Therefore, CeO_2 {111} facet has the highest stability, which is the most common crystal planes existing in nanoparticles. In addition, it has been reported that CeO_2 {111} is beneficial for photocatalysis. For example, Li et al. [29] proposed that the photo-generated electron migration on CeO_2 {111} facets is much more straight forward than {100}, leading to the decreased probability of recombination. Guo et al. [30] studied the effects of doping Pd, Ru and Cu in CeO_2 {111} on the adsorption, activation and reduction selectivity of CO_2, and showed that Cu/CeO_2 {111} has the highest reduction selectivity to CO_2. On the basis of that, it could be proposed that CeO_2 with {111} facet is a potential catalyst for CO_2

* Corresponding authors at: State Key Laboratory of Pollution Control and Resource Reuse, School of the Environmental, Nanjing University, Nanjing, 210023, PR China.
E-mail addresses: wxzou2016@nju.edu.cn (W. Zou), donglin@nju.edu.cn (L. Dong).

https://doi.org/10.1016/j.apcatb.2021.120257
Received 19 January 2021; Received in revised form 21 April 2021; Accepted 24 April 2021
Available online 26 April 2021

photo-reduction.

According to literature research, it is found that phosphate modification can significantly extend the photo-generated charge life of the catalyst, thereby improving its photocatalytic activity [31]. Bai et al. [32] prepared phosphate-modified g-C_3N_4 as a high efficiency photocatalyst for H_2O_2 production. They found that phosphoric acid modification enhanced the adsorption capacity of O_2 and increased the electron pair hole separation rate. Luan et al. [11] treated porous silica with appropriate amount of phosphoric acid, thus improving its photocatalytic activity for degrading gaseous acetaldehyde and liquid phenol (as colorless model pollutants). Phan et al. [15] successfully synthesized with phosphoric acid concentration by two solvent method Pt/H_3PO_4@MIL-101Cr catalysts. They showed that the total number of acid spots and its acid density on the surface of the catalyst increased significantly after modification with phosphoric acid.

Because of its attractive electronic structure, excellent chemical and thermal stability, and environmental friendliness, graphite carbonitrides (g-C_3N_4) are considered as promising two-dimensional nonmetallic materials in the fields of photocatalysis [33], electrocatalysis [34–36], and lithium-based batteries [37]. Moreover, g-C_3N_4 is a flexible support used to encapsulate semiconductor nanocrystals. Xu et al. [38] observed that g-C_3N_4 on graphite diacetylene nanocomposite could extend the life of photo-generated charge carrier and improve its photocatalytic H_2 production performance. Zhu et al. [39] proposed that the presence of g-C_3N_4 was beneficial for the multi-level electronic transfer on CeO_2@MoS_2/g-C_3N_4, in which a Z-scheme system is formed between MoS_2 and g-C_3N_4, leading to the fast transfer and separation of interface charges. Compared with the typical type-II heterojunction [40], at the interface of Z-scheme system, the photoelectrons in CB with lower reducibility and holes in VB with low oxidation would be recombined, and the electrons and holes with strong redox ability are beneficial for the activity [8].

Recently, the g-C_3N_4@CeO_2 catalysts with a higher superiority in photocatalytic CO_2 reduction have been reported [20,23,41]. However, little attention is paid to phosphate species modified CeO_2 {111}/g-C_3N_4 for photocatalytic CO_2 reduction, especially the role of phosphate. Therefore, in the work, we designed and fabricated phosphate on octahedral CeO_2 {111} surface coupled with g-C_3N_4 (P-CeO_2/g-C_3N_4) for photocatalytic CO_2 reaction, and the role of phosphate species was investigated in detail. Firstly, the coordination environment of P species was investigated by FT-IR, ^{1}H and ^{31}P solid-state MAS NMR, and the interfacial electronic interactions were explored by XPS and DFT calculation, which showed the bridge role of PO_4^{3-}. Under the strong interfacial electronic interaction, the Z-scheme formation and fast photo-generated charge transfer were present on P-CeO_2/g-C_3N_4. Secondly, the adsorption and activation process of CO_2 reactant molecules on catalyst surface were studied by CO_2-TPD. Finally, in-situ CO_2-adsorption DRIFTS under light irradiation were determined to propose the reaction mechanism for CO_2 photocatalytic reduction and the positive role of PO_4^{3-} in reaction sites. To our knowledge, the work provides a comprehensive understanding for the role of phosphate in the charge transport channel and reactant molecule adsorption/activation, both of which synergistically photocatalytic CO_2 reduction, and thus beneficial for the design and fabrication of high-efficient photocatalysts.

2. Experimental section

2.1. Materials

Urea, cerium nitrate hexahydrate ($Ce(NO_3)_3{\cdot}6H_2O$) and sodium phosphate tribasic dodecahydrate ($Na_3PO_4{\cdot}12H_2O$) were purchased from Sinopharm Chemical Reagent Co., Ltd. All chemicals are used of analytical grade.

2.2. Photocatalyst synthesis

2.2.1. P-CeO_2/g-C_3N_4

Graphite-like g-C_3N_4 was synthesized by directly heating urea at 550 ℃ for 4 h in a muffle furnace. The composite of P-CeO_2/g-C_3N_4 was obtained using a feasible hydrothermal treatment, and the mole ratio of CeO_2, carbon nitride and phosphate is 1: 4.72: 0.01. In detail, $Ce(NO_3)_3{\cdot}6H_2O$ (1 mmol) was dissolved in a mixture of g-C_3N_4 powder and deionized water (20 mL) under vigorous stirring and then $Na_3PO_4{\cdot}12H_2O$ (0.01 mmol) was slowly dispersed in 20 mL deionized water, which was added into the above mixture and stirred. Subsequently, the above mixture was sealed into a 50 mL Teflon-lined autoclave, followed by hydrothermal treatment at 170 ℃ for 17 h. The precipitates were separated by centrifuging, washed five times with deionized water and ethanol respectively, and fully dried in a vacuum oven at 60 ℃ for 12 h.

2.2.2. P-CeO_2

Phosphorus modified cerium oxide (P-CeO_2) was synthesized by the same method without g-C_3N_4. The pure CeO_2 could be obtained on the basis of P-CeO_2 by washing with deionized water and ethanol for many times until there was no phosphorus, as demonstrated by XPS analysis below.

2.3. Characterization

For photocatalyst, X-ray diffraction (XRD) was characterized on a Philips X'Pert Pro diffractometer under Ni-filtered Cu-Kα radiation ($\lambda = 1.5418$ nm). The morphologies and particle size of the synthesized catalysts were taken on a transmission electron microscopy (TEM, JEM-200CX) at 200 kV. Surface chemistry and VB were usually examined by XPS (ESCA PHI500). The optical properties of samples in the range of 200–800 nm were recorded by a UV–vis spectrophotometer diffuse reflectance spectroscopy (DRS, UV-3600Plus) with the reference of $BaSO_4$. Fourier transform infrared (FT-IR) spectra of samples within the range of 400–4000 cm^{-1} were analyzed by Nicolet5700 FT-IR spectrometer at the spectral resolution of 4 cm^{-1}. Photoluminescence (PL) spectra were carried out by a FluroMax-4 fluorescence spectrophotometer with an excitation wavelength of 325 nm at room temperature. The superoxide radicals were obtained at 77 K under visible light. CO_2-TPD experiment was carried out in a quartz U-tube reactor with a multifunction chemisorption analyzer (Tianjin Pengxiang, China) detected by the TCD. The 100 mg catalyst powder was heated to 200 °C for 1 h at a rate of 10 °C/min under N_2 flow, and then cooled to room temperature. After pretreatment, CO_2 flow passed through the catalyst bed for 30 min, subsequently followed by nitrogen flow to wash the sample for 60 min. Then, TPD results were obtained by heating 50 ℃ to 450 ℃ under N_2 flow at a heating rate of 10 ℃/min. The in-situ diffuse infrared Fourier transform (in-situ DRIFT) spectrum was recorded on a Nicolet 5700 FT-IR spectrometer with a frequency range of 1200–4000 cm^{-1} and a spectral resolution of 4 cm^{-1} (scanning times:32). The spectrometer was equipped with a highly sensitive mercury cadmium telluride detector, cooled by liquid N_2. The DRIFT cell (Harrick) was equipped with a KBr window and a heater, which could heat the sample to 400 °C. The catalyst powders placed on the sample stand were carefully smoothed to enhance the IR reflection. The samples were purged with N_2 flow at 150 °C to remove physically adsorbed water and other impurities. After pretreatment, the CO_2 flow was cooled to room temperature until saturation adsorption. Then the N_2 flow at room temperature was used to eliminate the physically adsorbed CO_2, and the DRIFTS spectra were measured. ^{1}H and ^{31}P solid-state MAS NMR measurements were performed on a Bruker avance III spectrometer. The photocatalytic active species of the system were explored through methylene blue (MB) degradation. Different scavengers such as isopropanol (IPA), ethylenediaminetetraacetic acid (EDTA), and benzoquinone (BQ) were used as the scavengers of hydroxyl (·OH), holes (h^+), and superoxide ($\cdot O_2^-$),

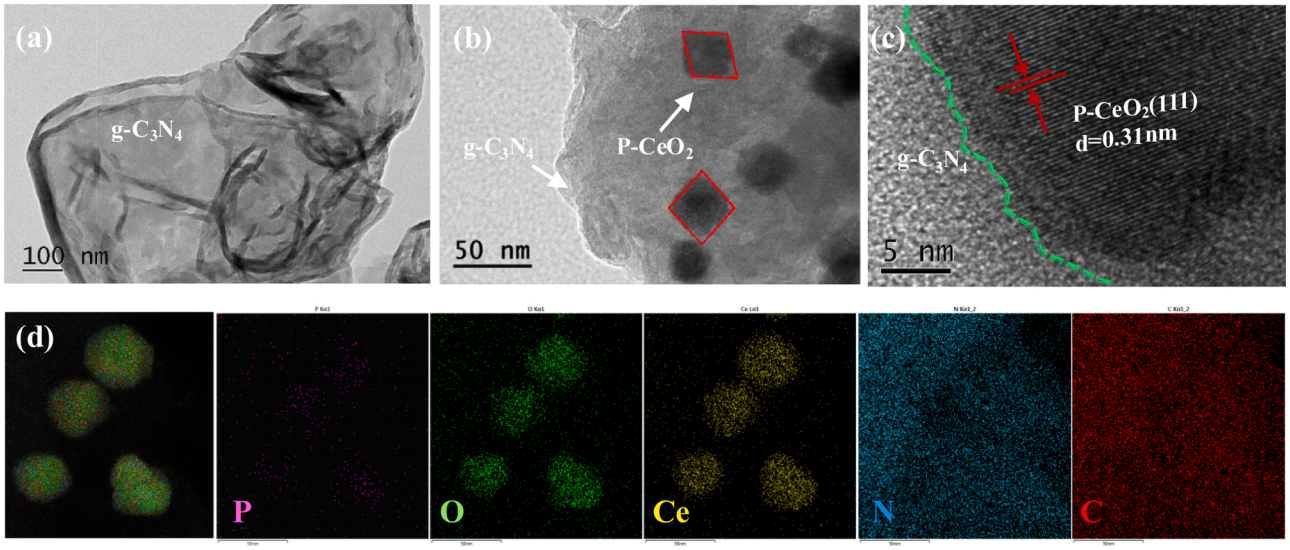

Fig. 1. TEM images of (a) g-C_3N_4 and (b) P-CeO_2/g-C_3N_4. (c) The HRTEM image of P-CeO_2/g-C_3N_4. (d) The corresponding element-sensitive mapping images of P, O, Ce, N, C of P-CeO_2/g-C_3N_4.

respectively.

2.4. Electrochemical measurements

The light wavelength of full spectrum in electrochemical measurements (including photocurrent and electrochemical impedance spectroscopy (EIS) measurements) on a CHI660E electrochemical workstation were carried out on a standard three-electrode cell. Fluorine-doped tin oxide, Hg/Hg_2Cl_2 electrode and platinum wire electrode were used as the working electrode, reference electrode and counter electrode of the sample. 0.1 M Na_2SO_4 and Xe lamp were uesd as the electrolyte solution and light source, respectively.

2.5. Photocatalytic test

The photocatalytic reduction of CO_2 was carried out in a 50 mL Teflon-lined autoclave, using a 300 W Xe lamp as light source. Typically, the catalyst powder (50 mg) was uniformly dispersed in 5 mL of distilled water and high purity of CO_2 gas was added up to 4 bar. The suspension was stirred for 30 min and then irradiated with full spectrum for 8 h. The CO product was monitored at a 120 min interval by an online gas chromatograph. In addition, a cycle experiment was conducted, with each cycle lasting 8 h. After each cycle, the used sample was washed several times in distilled water and then dried in an oven at 80 °C.

2.6. DFT calculation

All the spin theoretical simulations in our work were carried out on the Vienna ab initio Simulation Package (VASP) with the version 5.4.1. The Generalized gradient approximation (GGA) with the Perdew-Burke-Emzerhof (PBE) functional form was employed to evaluate the electron-electron exchange and correlation interactions while the projector augmented-wave (PAW) methods were implanted to represent the core-electron (valence electron) interactions. Plane-Wave basis function was set with a kinetic cut-off energy of 400 eV. The ground-state atomic geometries were optimized by relaxing the force below 0.02 eV/Å and the convergence criteria for energy was set with the value of 1.0×10^{-5} eV/cell. A Monkhorst-Pack meshes with the size of $3 \times 3 \times 1$ were employed to slab models Brillouin zone for our calculations. Gaussian method was employed for the stress/force relaxations total energy, and electronic structures.

3. Results and discussion

3.1. Morphological and structural information

The morphologies and nanostructures of bare g-C_3N_4 and P-CeO_2/g-C_3N_4 composite were investigated by TEM as demonstrated in Fig. 1. The layered structure of g-C_3N_4 was observed in the TEM (Fig. 1a) image, because of its planar graphitic-like structure. In Fig. 1b, it can be apparently observed that g-C_3N_4 acts as a flexible support and the P-CeO_2 nanoparticles with octahedral morphology are uniformly loaded on the g-C_3N_4 sheets [42]. Moreover, the HRTEM image was used to explore the exposed crystal plane of P-CeO_2. In Fig. 1c, the lattice spacing is 0.31 nm, corresponding to the {111} plane of CeO_2, while the blurred area below the indigo dotted line is g-C_3N_4 due to its poor crystallinity [43]. It can be clearly seen that the octahedral P-CeO_2 {111} and g-C_3N_4 are closely combined to form a heterojunction structure, which is considerable for the electron transfer at the interface between heterojunction structure [44]. Besides, the energy dispersive X-ray spectroscopy mapping (Fig. 1d) further shows that elements, including P, O, Ce, N, and C, are homogenously distributed on the composite material, and most of the P is loaded on CeO_2 surface, indicating a close interfacial contact between P-CeO_2 and g-C_3N_4.

The phase structures of g-C_3N_4, CeO_2, P-CeO_2, and P-CeO_2/g-C_3N_4 composites were investigated by XRD characterization. As shown in **Fig. S1**, as for g-C_3N_4, the characteristic peak around 27.7° is assigned to the (002) diffraction planes and corresponded to interlayer stacking of aromatic segments. Additionally, the intensity of the diffraction peaks at *ca.* 28.6°, 33.3°, 47.5°, 56.2° are indexed as the (111), (222), (200), (311) crystal planes of the CeO_2 (JCPDS no:04-0802), respectively. In P-CeO_2/g-C_3N_4 composites, the XRD pattern is similar to CeO_2, and the characteristic peaks belonging to g-C_3N_4 are missing,which is possible that the relatively diffraction intensity of CeO_2 is too strong and it masks the signal of g-C_3N_4. To confirm the presence of both g-C_3N_4 and P in the obtained P-CeO_2/g-C_3N_4 composites, FT-IR analysis and ICP were further performed. Obviously, in **Fig. S2**, the significant peak at 808 cm^{-1} is ascribed to the bending pattern of the heptazine ring of g-C_3N_4 and the peaks in the range of 1700–1200 cm^{-1} are typical tensile vibrations of g-C_3N_4 [32,45]. Moreover, the existing of P was determined from ICP technology, and the mass ratio of P/Ce is close to the experimental input ratio of 0.22 (**Table S1**). On the basis of TEM, XRD, FT-IR and ICP results, it is suggesting that phosphate modified octahedral CeO_2 {111} manoparticles are successfully loaded on the g-C_3N_4

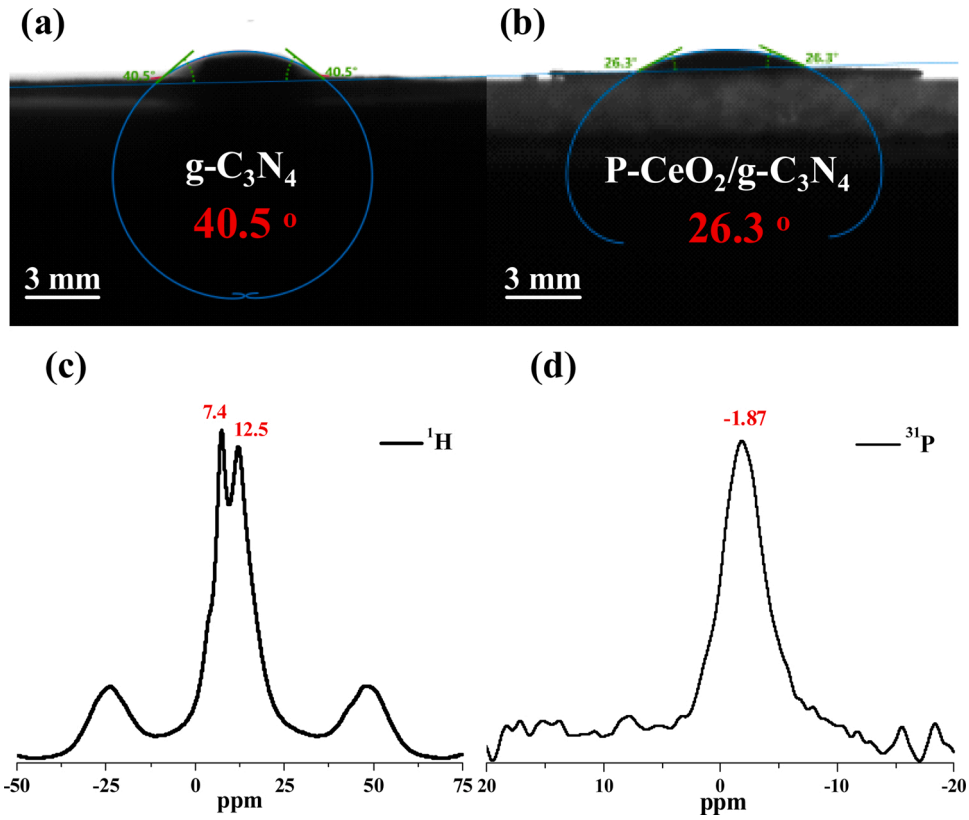

Fig. 2. The contact angle results of (a) g-C_3N_4 and (b) P-CeO_2/g-C_3N_4; (c) ^1H MAS NMR result of P-CeO_2/g-C_3N_4; (b) ^{31}P MAS NMR result of P-CeO_2/g-C_3N_4.

supports.

3.2. Phosphate coordination environment and interfacial electronic interaction

Generally, the interfacial electronic interaction, related to the

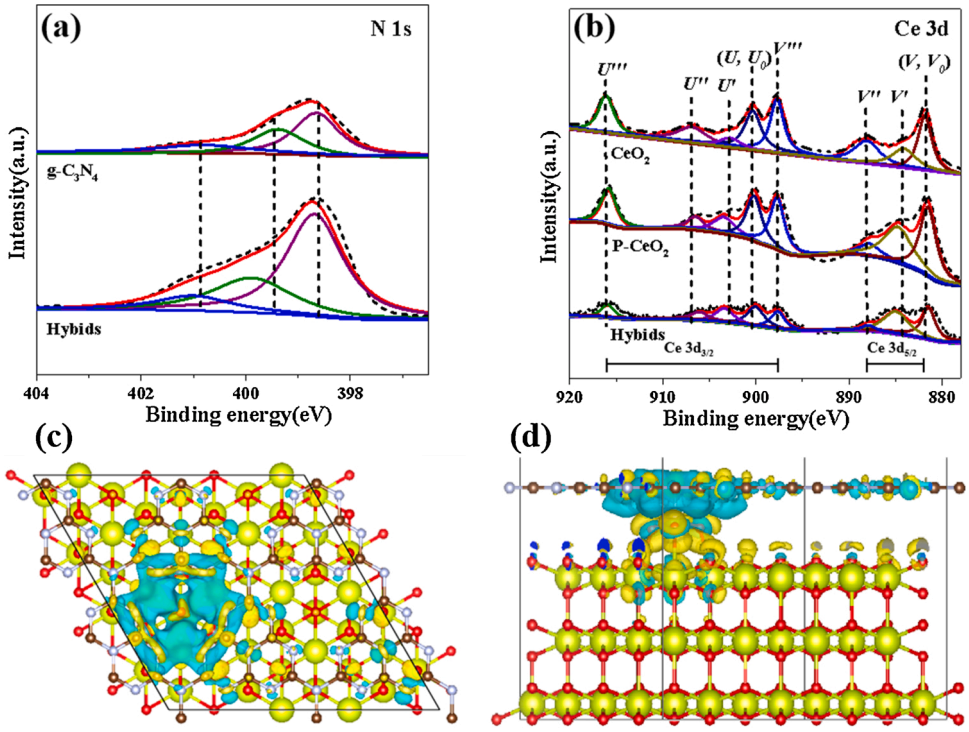

Fig. 3. High-resolution XPS images of (a) N 1s, and (b) Ce 3d for g-C_3N_4, CeO_2, P-CeO_2 and P-CeO_2/g-C_3N_4. (c-d) DFT calculation of P-CeO_2/g-C_3N_4.

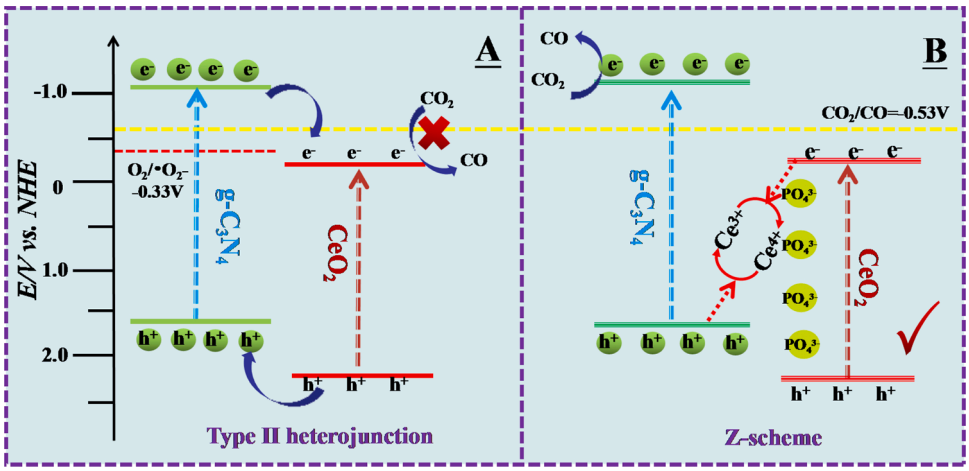

Fig. 4. Schematic diagram of photoinduced electron-hole separation process for P-CeO_2/g-C_3N_4 Z-scheme heterojunction.

surface electronic structures and coordination states, is beneficial for the photocatalytic performance. Therefore, the phosphate coordination environment was investigated via contact angle measurement, FT-IR, XPS and ^{1}H and ^{31}P solid-state MAS NMR, in order to explore the interfacial electronic interactions of P-CeO_2/g-C_3N_4 composites. Moreover, the contact angle of P-CeO_2 was determined and showed in **Fig. S3**. It was proposed that P-CeO_2 modified g-C_3N_4, and thus the contact angle of P-CeO_2/g-C_3N_4 is reduced from 40.5° (g-C_3N_4) to 26.3° (Fig. 2a and b), indicating that the hydrophilicity of the composite is better, and more oxygen-containing species are present on P-CeO_2/g-C_3N_4. The XPS spectra of O 1s also suggests the above phenomenon. The wide peak in (**Fig. S4**) is fitted into three peaks, and the peaks at 528.6 and 531.1 eV are attributed to the lattice oxygen and chemisorbed oxygen of CeO_2, respectively. Based on the calculated peak area values of $I_{(H2O+OH)}/I_{lattice}$ (**Table S3**), P-CeO_2/g-C_3N_4 surface is provided with richer chemisorbed oxygen species, further verifying that more oxygen-containing species are present on P-CeO_2/g-C_3N_4.

The FT-IR spectra proposed the existing state of the surface absorbed oxygen-containing species. In **Fig. S2**, the broad peaks between 3500 and 3000 cm^{-1} ascribed to surface absorbed function groups [50] became broaden and weaken on P-CeO_2/g-C_3N_4 interface, suggesting that the hydrogen bonding between phosphate and amino groups might be present. Furthermore, ^{1}H and ^{31}P solid-state MAS NMR were employed to investigate the existing state and coordination environment of phosphate. In the ^{1}H MAS NMR (Fig. 2c), the two signals located at 7.4 and 12.5 ppm correspond to hydrogen bonds in amino groups, and P—OH, respectively [46]. In addition, the signal at -1.87 ppm in the ^{31}P MAS NMR (Fig. 2d) is attributed to the HPO_4^{2-} species [47]. Combined with the results of XPS and NMR, it could be proposed that on P-CeO_2/g-C_3N_4 interface, the hydrogen bonds between phosphate and amino groups are present.

Moreover, XPS and DFT calculations investigated the electronic interactions via hydrogen bonds between the P-CeO_2/g-C_3N_4 interface. According to the literature, the C 1s XPS spectra (**Fig. S5a**) of P-CeO_2/g-C_3N_4 and g-C_3N_4 can be deconvoluted into two peaks, which are assigned to 284.6 eV for graphitic C—C bond and 287.9 eV for N—C═N bond of g-C_3N_4, respectively [9]. And the N 1s XPS spectra of P-CeO_2/g-C_3N_4 and g-C_3N_4 fitted with three peaks are attributed to 398.7 eV of C═N—C groups in the triazine rings, 399.4 eV of N-C_3 groups and 400.8 eV of C-*N*-H, respectively, as depicted in Fig. 3a [48]. It was found that, compared to the pure g-C_3N_4, the binding energies of XPS spectra of N 1s are shifted to the higher values on P-CeO_2/g-C_3N_4, suggesting that less electrons were on CN rings of P-CeO_2/g-C_3N_4. The Ce 3d spectra (Fig. 3b) were determined to show the above phenomenon. Compared to the pure CeO_2 and P-CeO_2, the binding energies attributed to Ce species on P-CeO_2/g-C_3N_4 are shifted to low values, showing that more electrons accumulate on Ce species of P-CeO_2/g-C_3N_4, due to the interfacial electrons donating from g-C_3N_4 to P-CeO_2. In addition, the XPS spectra of P 2p also showed the above interfacial electrons transfer process. According to the references [12, 49,50], the XPS spectra of P 2p (**Fig. S5b**) has been fitted into three peaks, i.e., the peaks at *ca.* 133.4, 134.1 and 135.1 eV are attributed to HPO_4^{2-}, PO_4^{3-} and P═O bond, respectively. Combined with the results of ^{31}P MAS NMR (Fig. 2d) and the interfacial electronic interaction (Fig. 3d), the XPS peak of P-CeO_2/g-C_3N_4 at *ca.*133.8 eV is attributed to HPO_4^{2-}. Interestingly, on P-CeO_2/g-C_3N_4, the binding energy is shifted to higher value, further showing that on the formed interfacial built-in field, the electron direction is transferred from g-C_3N_4 to CeO_2 via the phosphate bridge.

Furthermore, in order to better characterize and confirm the electron direction of the interfacial built-in field on P-CeO_2/g-C_3N_4, the difference in charge densities of P-CeO_2 and g-C_3N_4 are calculated through DFT method, as shown in Fig. 3c and d. In the diagram, cyan and yellow colors represented a decrease and increase in electron density, respectively. Based on this, it is observed that a large number of electrons accumulate on CeO_2, while electrons decrease on g-C_3N_4, which indicate that electrons are transferred from g-C_3N_4 to CeO_2 through the PO_4^{3-} bridge, leading to the formed interfacial built-in field on P-CeO_2/g-C_3N_4.

3.3. Band structure and photo-generated charge transfer

Since band structures of photocatalysts play an important role in the photocatalysis, which could be studied by UV–vis DRS and XPS-valence band (VB) spectra. As shown in **Fig. S6a**, the band gap energies are calculated according to the extrapolation of absorption edge and the equation E_g=1240/λ. The pure g-C_3N_4 and P-CeO_2 bandgap values are calculated to be about 2.69 and 2.57 eV, respectively. Besides, the XPS-VB spectra of samples were determined in **Fig. S7**. Based on the equation of $E_{CB}=E_{VB}-E_g$, the conduction band minimum (CBM) can be calculated to be −1.08 eV for g-C_3N_4 and −0.23 eV for P-CeO_2, respectively (**Table S4**), which were closed to the Mott Schottky results of g-C_3N_4 and P-CeO_2 (**Fig. S8**), that are, −1.10 and −0.25 eV, respectively.

Considering of the built-in electronic field and band structures of P-CeO_2/g-C_3N_4, it is proposed that Z-scheme heterojunction is present. In order to further verify the Z-scheme mentioned above, the photocatalytic active species of the system were explored through methylene blue (MB) degradation. Different scavengers such as isopropanol (IPA), ethylenediaminetetraacetic acid (EDTA), and benzoquinone (BQ) were used as the scavengers of hydroxyl (·OH), holes (h^+), and superoxide ($\cdot O_2^-$), respectively [8]. It was well known that the study of the main active species in the photocatalytic degradation process could play an important role in deriving the charge transfer pathway of composite

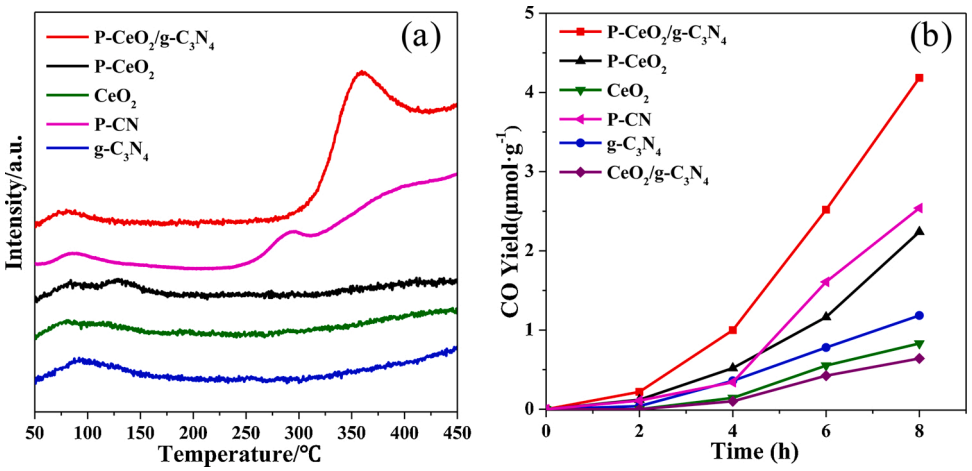

Fig. 5. (a) CO_2-TPD; (b) CO production of P-CeO_2/g-C_3N_4, P-CeO_2, P-CN, CeO_2, g-C_3N_4.

materials [51]. As shown in **Fig. S9a**, the addition of IPA has little effect on the photocatalytic degradation rate of methylene blue, while the introduction of EDTA or BQ has obvious changes. Therefore, we preliminarily infers that h^+ and $\cdot O_2^-$ can promote the degradation of methylene blue. Furthermore, the active species of P-CeO_2 and g-C_3N_4 are h^+ and $\cdot O_2^-$, respectively (**Fig. S9b and c**), which are consistent with the active species of P-CeO_2/g-C_3N_4. In other words, only when the electrons and holes in P-CeO_2/g-C_3N_4 migrate in accordance with the Z-heterojunction mechanism, electrons can be enriched on CB of g-C_3N_4, and holes are accumulated on VB of P-CeO_2, as shown in Fig. 4b. However, if P-CeO_2/g-C_3N_4 photocatalyst has type II structure (Fig. 4a), the E_{CB} edge potential of P-CeO_2 (−0.23 V vs NHE) is more positive than $E(CO_2/CO)$ (−0.53 V vs NHE), which is not conducive to the reduction of CO_2 to CO. Therefore, it could be reasonably concluded that the direct Z-scheme photocatalysis system was formed in P-CeO_2 to g-C_3N_4, instead of a type-II scheme.

Under the interfacial electronic interactions and built-in electronic field, P-CeO_2/g-C_3N_4 with the Z-scheme heterojunction is provided with fast photo-generated charge transfer. Photoluminescence (PL) spectra, transient photocurrent responses and electrochemical impedance spectroscopy (EIS) Nyquist plots were used to suggest the fast charges migration and low electron-hole recombination. **Fig. S6b** depicts that the pure CeO_2 shows a highly strong PL intensity under the excitation of 325 nm laser, and its emission band is concentrated at about 450 nm, which can be attributed to its rapid electron-hole recombination. However, the PO_4^{3-} modification and the formation of heterostructures promote the charge transport at the heterojunction interface and considerably slow down the recombination rate of photogenerated carriers. Therefore, the P-CeO_2/g-C_3N_4 composite has the lowest PL intensity and photo-generated charge recombination. The transient photocurrent responses of the bare CeO_2, pure g-C_3N_4, P-CeO_2, and P-CeO_2/g-C_3N_4 were showed in **Fig. S6c**. It is well-known that the higher photocurrent intensity indicates that a large number of charge carriers will be generated quickly, and their separation and transmission can be effectively achieved [52]. Compared with the bare CeO_2, pure g-C_3N_4 and P-CeO_2, the P-CeO_2/g-C_3N_4 composite shows the highest photocurrent response intensity, which is about 2.5 times of CeO_2, 1.5 times of g-C_3N_4 and 1.7 times of P-CeO_2. Furthermore, we employed EIS as shown in **Fig. S6d** to confirm this result. Compared with other single components, the semicircle of the Nyquist curve of the P-CeO_2/g-C_3N_4 composite material is significantly reduced, showing the shortest semicircle, which indicates that the charge-transfer process is accelerated due to the PO_4^{3-} bridge and the interfacial electronic interactions. Therefore, due to the role of interfacial electronic effects, the P-CeO_2/g-C_3N_4 with Z-scheme heterojunction are formed, which has the ability to efficiently promote the migration of photoinduced electrons and holes.

3.4. CO_2 adsorption/activation and photocatalytic performance

In general, the adsorption and activation process of reactant molecules on the catalyst surface was of great significance to photocatalysis. Herein, the CO_2-TPD characterization was used to analyze the interaction between CO_2 reactant and photocatalysts. As shown in Fig. 5a, it can be found that P-CeO_2 adsorbs more CO_2 than pure CeO_2, indicating that phosphate modification is beneficial to adsorbing more reactants. Obviously, the CO_2-TPD results show a wide peak in the temperature range of 50–450 ℃, which is attributed to the CO_2 adsorbed on the catalyst surface and the reaction intermediates (carbonate species). According to the present study [16,17], the broad peak is divided into several adsorbed species: molecule-adsorbed CO_2 (50–180 °C), HCO_3^- or carboxylate (180–370 °C), bicondentate carbonates (b−CO_3^{2-}, 370–550 °C) and monondentate carbonates (m−CO_3^{2-}, 550–780 °C). Among them, the formation of HCO_3^- species is due to the interaction between the surface hydroxyl group and CO_2, while the formation of b−CO_3^{2-} and m−CO_3^{2-} is resulted from the combination of CO_2 molecules with the surface oxygen or metal atoms of the catalysts. It can be observed that the P-CeO_2/g-C_3N_4 and P-CN compounds show a wide peak at 180–450 ℃, corresponding to HCO_3^- and b−CO_3^{2-} species with moderate strong basicity. The peak strength of P-CeO_2/g-C_3N_4 is higher than that of P-CN, based on the consistent content of the testing that, it is proposed that P-CeO_2/g-C_3N_4 is beneficial for the adsorption of CO_2 molecules. In addition, the reaction performance of CO_2 reduction confirms that P-CeO_2/g-C_3N_4 is provided with the best photoactivity than others. Combined with the above-mentioned XPS of O 1s, the PO_4^{3-} modification generates more oxygen containing species, which are provided with more lone pair of electrons and then act as the Lewis basic sites for adsorption and activation CO_2 molecules.

Furthermore, the photoreduction of CO_2 was carried out under full spectrum radiation, and the photocatalytic activities of pure g-C_3N_4, bare CeO_2, P-CeO_2 and P-CeO_2/g-C_3N_4 nanocomposites were evaluated under the same conditions for comparison, as shown in Fig. 5b. The highest CO production rate of the P-CeO_2/g-C_3N_4 composite is 4.184 μmol g^{-1}, which is 3.5, 5, 1.6 and 1.8 times higher than g-C_3N_4, CeO_2, P-CN and P-CeO_2, respectively. In addition, the CO yield of CeO_2/g-C_3N_4 is significantly lower than that of P-CeO_2/g-C_3N_4, suggesting that superiority of the PO_4^{3-} bridge modificated P-CeO_2/g-C_3N_4 can enhance the intensive interfacial electronic interactions, Z-scheme heterojunction formation and more Lewis basic sites. The related blank tests were determined as following processes, respectively: (1) with the catalyst, CO_2 and H_2O, the reaction system stirred in dark; (2) with CO_2 and H_2O, the reaction system stirred under light irradiation without

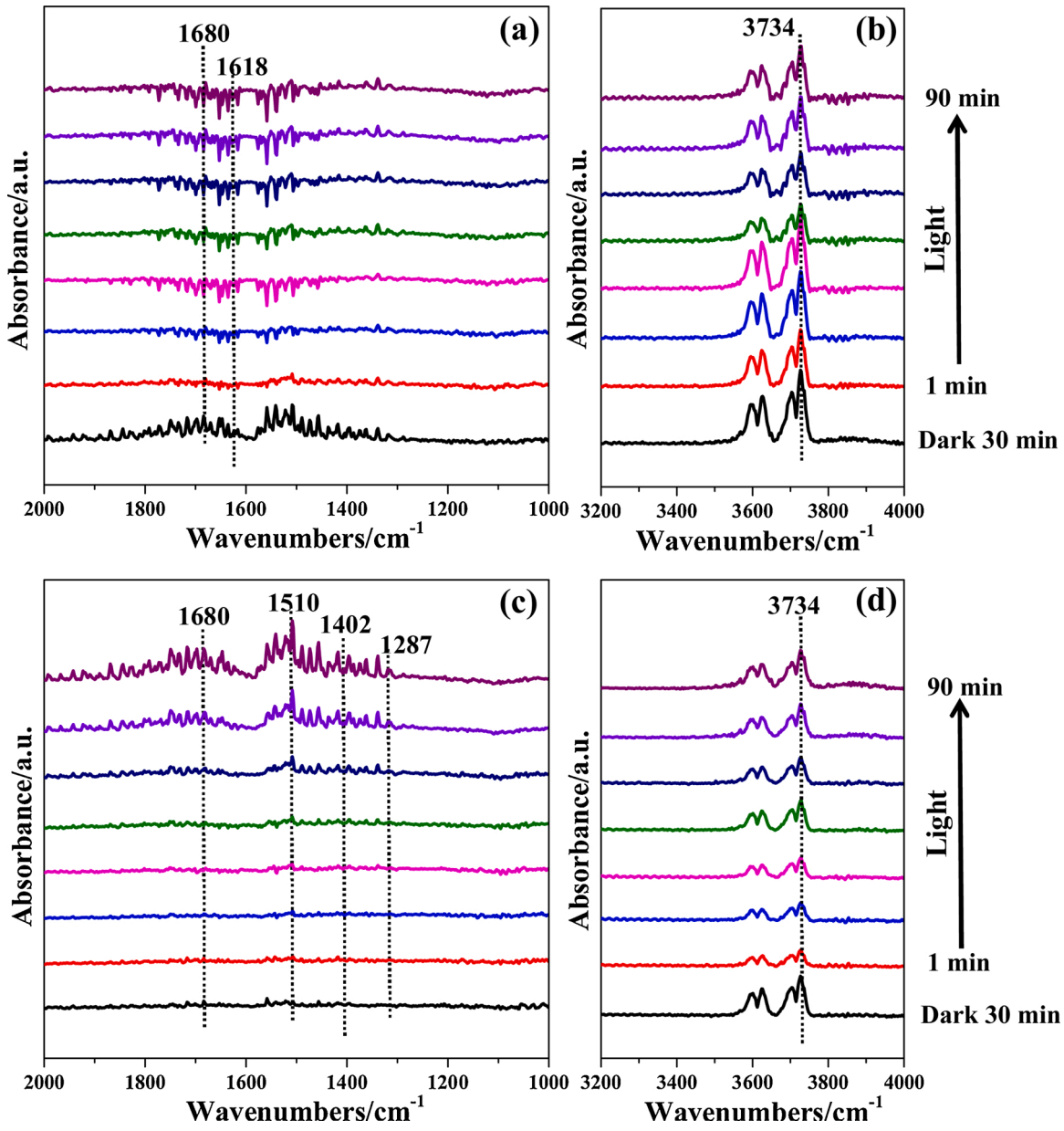

Fig. 6. CO_2 adsorption DRIFTS of (a) (b) P-CeO_2/g-C_3N_4 and (c) (d) CeO_2/g-C_3N_4.

catalyst; (3) with the catalyst and H_2O, the reaction system stirred under light irradiation without CO_2. From the above three processes, no obvious CO production was observed, respectively (**Fig. S10**). On the basis of the result of blank tests, it could be believed that the CO was from the CO_2 reactant. The photostability of P-CeO_2/g-C_3N_4 is of great importance in practical applications, and thus the stability of the best P-CeO_2/g-C_3N_4 compound was operated by three cycles of photocatalytic reduction of CO_2. Therefore, we have conducted the XRD spectra of P-CeO_2/g-C_3N_4 before and after the reactions. Apparently, the XRD results (**Fig. S12**) exhibit that no noticeable change of the crystal phase can be observed in the fresh and reused composite. In addition, the recycling rest of CO production (**Fig. S11**) indicated that the photocatalytic activity of P-CeO_2/g-C_3N_4 remained almost unchanged after the reaction. Thus, it can be concluded that the P-CeO_2/g-C_3N_4 heterojunction is stable. Moreover, the photocatalytic CO_2 reduction performance of other related materials in literatures are compared in **Table S2**. In a word, the P-CeO_2/g-C_3N_4 composite has some advantages in the application of the photocatalytic CO_2 reduction.

3.5. Proposed mechanism of CO_2 photoreduction

In order to describe the CO_2 adsorption/activation process and determine reactant active sites on P-CeO_2/g-C_3N_4, the in-situ CO_2 adsorption DRIFTS under light irradiation were performance on P-CeO_2/g-C_3N_4 and CeO_2/g-C_3N_4 samples to explore the reaction mechanism. As shown in the Fig. 6, after CO_2 adsorption is saturated under dark conditions, carboxylate CO_2^- (1680 cm^{-1}) and HCO_3^- (1618 cm^{-1}) [18,19] are generated on the P-CeO_2/g-C_3N_4 surface. According to the literature [21], the appearance of carboxylate and HCO_3^- species means that the activation of CO_2 is easier, that is, P-CeO_2/g-C_3N_4 is more facilitate to adsorption and activation of CO_2 reactant, consistent to the CO_2-TPD result. After exposure to light (**Fig. S13**), the amounts of CO_2 on the P-CeO_2/g-C_3N_4 sample gradually decrease, at the same time, the peak in the region of 3600–3740 cm^{-1} weakened, indicating that the adsorbed CO_2 and hydroxyl species [53] participated in the reaction. Whereas, for CeO_2/g-C_3N_4 sample, no absorbed carbonate species are observed under dark conditions. Once under light irradiation, the carboxylate CO_2^- (1680 cm^{-1}) and monodentate carbonate (1510, 1402

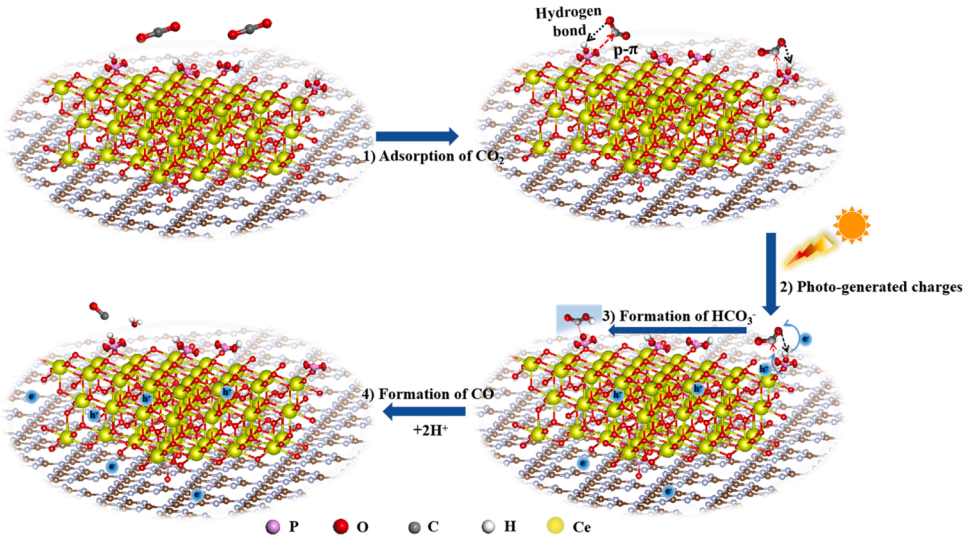

Fig. 7. The possible reaction mechanism of the CO_2 photoreduction on P-CeO_2/g-C_3N_4 samples.

and 1287 cm^{-1}) are generated, suggesting that after light irradiation, CeO_2/g-C_3N_4 sample has less ability for the CO_2 adsorption. In addition, the peak intensities of CO_2 with light exposure times on the CeO_2/g-C_3N_4 surface are hardly changed. Different from P-CeO_2/g-C_3N_4, which confirms that the photoreduction reaction of CO_2 undergoes slower and CO_2 is hard to activation on CeO_2/g-C_3N_4. Therefore, it can be explained that the performance of P-CeO_2/g-C_3N_4 composite is great because HCO_3^- species play a key role in the activation process, due to the surface Lewis basic sites, which is easier to produce CO.

The process mechanism of Fig. 7 were involved of four processes as followed: (1) CO_2 reactant molecules are adsorbed on P-CeO_2/g-C_3N_4, i.e., hybrid of empty orbitals of C atoms (CO_2) and 2p orbitals of O atoms (P-CeO_2), hydrogen bonds of O atoms (CO_2) and H atoms of amino groups (g-C_3N_4). (2) Under light irradiation, photo-electrons and holes are generated on g-C_3N_4 and P-CeO_2, respectively. The photo-generated electrons transfer to the hydrogen bonds of amino groups (g-C_3N_4) and O atoms (CO_2). (3) Under the above electronic interactions, HCO_3^- intermediate active species are generated. (4) Under the attack of hydrogen protons on oxygen atoms (HCO_3^- intermediate and PO_4^{3-}), the CO production is formed.

4. Conclusions

In the work, the P-CeO_2/g-C_3N_4 photocatalyst were obtained and had the superior photocatalytic performance of CO_2 reduction. In the role of PO_4^{3-}, interfacial electronic effects promoted Z-scheme formation and fast photo-induced charge transfer. In addition, PO_4^{3-} modification enhanced the Lewis basic sites to CO_2 adsorption and activation, and in-situ CO_2 adsorption DRIFTS under light irradiation proposed the reaction mechanism, i.e., the synergistic effects of the directional charge-transfer channel and abundant active sites on P-CeO_2/g-C_3N_4 photocatalyst.

CRediT authorship contribution statement

Wanqin Li: Conceptualization, Investigation, Visualization, Writing - original draft. **Li Jin:** Investigation. **Fei Gao:** Visualization. **Haiqin Wan:** Investigation. **Yu Pu:** Data curation. **Xiaoqian Wei:** Software. **Chong Chen:** Investigation. **Weixin Zou:** Supervision, Conceptualization, Resources, Project administration, Writing - review & editing. **Chengzhang Zhu:** Software, Writing - review & editing. **Lin Dong:** Supervision, Project administration, Writing - review & editing.

Declaration of Competing Interest

The authors declare no conflict of interest.

Acknowledgements

The authors gratefully acknowledge the financial support from the National Natural Science Foundation of China (21976082, 21972062, and 21908092) and the Natural Science Foundation of Jiangsu Province (BK20200012).

Appendix A. Supplementary data

Supplementary material related to this article can be found, in the online version, at https://doi.org/10.1016/j.apcatb.2021.120257.

References

[1] F. Chen, Z.Y. Ma, L.Q. Ye, T.Y. Ma, T.R. Zhang, Y.H. Zhang, H.W. Huang, Macroscopic spontaneous polarization and surface oxygen vacancies collaboratively boosting CO2 photoreduction on BiOIO3 single crystals, Adv. Mater. (2020), 1908350.
[2] L. Hao, L. Kang, H.W. Huang, L.Q. Ye, K.L. Han, S.Q. Yang, H.J. Yu, M. Batmunkh, Y.H. Zhang, T.Y. Ma, Surface-halogenation-Induced atomic-site activation and local charge separation for superb CO2 photoreduction, Adv. Mater. 31 (2019), 1900546.
[3] S.B. Wang, X. Han, Y.H. Zhang, N. Tian, T.Y. Ma, H.W. Huang, Inside-and-Out semiconductor engineering for CO2 photoreduction: from recent advances to new trends, Small Structures 2 (2021), 2000061, https://doi.org/10.1002/sstr.202000061.
[4] H. Wu, Y.J. Li, H.M. Liu, D.H. He, High-pressure catalytic kinetics of CO2 reforming of methane over highly stable NiCo/SBA-15, Catal. ES Energy Environ. 3 (2019) 68–73.
[5] A.W. Dong, T.T. Dai, M.Y. Ren, X.M. Zhao, S.L. Zhao, Y.H. Yuan, Q. Chen, N. Wang, Functionalization and fabrication of soluble polymers of intrinsic microporosity for CO2 transformation and uranium extraction, Eng. Sci. 5 (2019) 56–65, https://doi.org/10.30919/es8d613.
[6] A.W. Dong, Y.Q. Zhu, M.Y. Ren, X.Y. Sun, V. Murugadoss, Y.H. Yuan, J. Wen, X. L. Wang, Q. Chen, Z.H. Guo, N. Wang, Remarkably enhanced CO2 uptake and uranium extraction by functionalization of cyano-bearing conjugated porous polycarbazoles, Eng. Sci. 6 (2019) 44–52.
[7] X.M. Xiang, F.P. Pan, Y. Li, A review on adsorption-enhanced photoreduction of carbon dioxide by nanocomposite materials, Adv. Compos. Hybrid Mater. 1 (2018) 6–31.
[8] X. Wang, G. Liu, Z.G. Chen, F. Li, L. Wang, G.Q. Lu, H.M. Cheng, Enhanced photocatalytic hydrogen evolution by prolonging the lifetime of carriers in ZnO/CdS heterostructures, Chem. Commun. 23 (2009) 3452–3454.
[9] F. Guo, M.Y. Li, H.J. Ren, X.L. Huang, K.K. Shu, W.L. Shi, C.Y. Lu, Facile bottom-up preparation of Cl-doped porous g-C3N4 nanosheets for enhanced photocatalytic degradation of tetracycline under visible light, Sep. Purif. Technol. 228 (2019), 115770.

[10] C.L. Jiang, H. Wang, Y.Q. Wang, H.B. Ji, All solid-state Z-scheme CeO2/ZnIn2S4 hybrid for the photocatalytic selective oxidation of aromatic alcohols coupled with hydrogen evolution, Appl. Catal. B 277 (2020), 119235.
[11] Y.B. Luan, Y.J. Feng, H.Q. Cui, Y. Cao, L.Q. Jing, Enhanced photocatalytic activity of P25 TiO2 after modification with phosphate-treated porous SiO2, Chem. Plus Chem. 79 (2014) 1271–1277, https://doi.org/10.1002/cplu.201402063.
[12] H.C. Keng, B.P. Moreica, C. Wen-Fan, K. Pramod, C.S. Charles, Thermodynamic and microstructural analyses of photocatalytic TiO2 from the anodization of biomedical-grade Ti6Al4V in phosphoric acid or sulfuric acid, Ceram. Int. 47 (2021) 1609–1624.
[13] Q.C. Gao, Z.M. Yuan, G.H. Yang, Z.J. Tian, Z.Y. Jiang, K. Zhang, C. Wang, J. C. Chen, Enhancement of lignin-based carbon quantum dots from poplar pre-hydrolysis liquor on photocatalytic CO2 reduction via TiO2 nanosheets, Ind. Crops Prod. 9 (2020), 113161.
[14] Z.K. Xie, Y.Y. Xu, D. Li, L.J. Chen, S.C. Meng, D.L. Jiang, M. Chen, Construction of CuO quantum Dots/WO3 nanosheets 0D/2D Z-scheme heterojunction with enhanced photocatalytic CO2 reduction activity under visible-light, J. Alloys. Compd. 8 (2020).
[15] D.P. Phan, E.Y. Lee, Phosphoric acid enhancement in a Pt-encapsulated Metal-Organic Framework (MOF) bifunctional catalyst for efficient hydro-deoxygenation of oleic acid from biomass, J. Catal. 386 (2020) 19–29.
[16] Y. Pu, Y.D. Luo, X.Q. Wei, J.F. Sun, L.L. Li, W.X. Zou, L. Dong, Synergistic effects of Cu2O-Decorated CeO2 on photocatalytic CO2 reduction: surface lewis Acid/Base and oxygen defect, Appl. Catal. B 254 (2019) 580–586.
[17] J. Zhao, Y. Wang, Y.X. Li, X. Yuea, C.Y. Wang, Phase-dependent enhancement for CO2 photocatalytic reduction over CeO2/TiO2 catalysts, Catal. Sci. Technol. 6 (2016) 7967–7975.
[18] C.Z. Zhu, X.Q. Wei, W.Q. Li, Y. Pu, J.F. Sun, K.L. Tang, H.Q. Wan, C.Y. Ge, W. X. Zou, L. Dong, Crystal-plane effects of CeO2 {110} {100} on photocatalytic CO2 reduction: synergistic interactions of oxygen defect and hydroxyl group, ACS Sustain. Chem. Eng. 8 (38) (2020) 14397–14406.
[19] Y. Wang, J. Zhao, T.F. Wang, Y.X. Li, X.Y. Li, J. Yin, C.Y. Wang, CO2 photoreduction with H2O vapor on highly dispersed CeO2/TiO2 catalysts: surface species and their reactivity, J. Catal. 337 (2016) 293–302.
[20] M.F. Liang, T. Borjigin, Y.H. Zhang, B.H. Liu, H. Liu, H. Guo, Controlled assemble of hollow heterostructured g-C3N4@CeO2 with rich oxygen vacancies for enhanced photocatalytic CO2 reduction, Appl. Catal. B 243 (2019) 566–575.
[21] C. Luo, J. Zhao, Y.X. Li, W. Zhao, Y.B. Zeng, C.Y. Wang, Photocatalytic CO2 reduction over SrTiO3: correlation between surface structure and activity, Appl. Surf. Sci. 447 (2018) 627–635.
[22] Z. Xiong, Z. Lei, Z.W. Xu, X.X. Chen, B.G. Gong, Y.C. Zhao, H.B. Zhao, J.Y. Zhang, C.G. Zheng, Flame spray pyrolysis synthesized ZnO/CeO2 nanocomposites for enhanced CO2 photocatalytic reduction under UV-Vis light irradiation, J. CO2 Util. 18 (2017) 53–61.
[23] M.L. Li, L.X. Zhang, M.Y. Wu, Y.Y. Du, X.Q. Fan, M. Wang, L.L. Zhang, Q.L. Kong, J. L. Shi, Mesostructured CeO2/g-C3N4 nanocomposites: remarkably enhanced photocatalytic activity for CO2 reduction by mutual component activations, Nano Energy 19 (2016) 145–155.
[24] Y.Y. Cui, W.L. Dai, Support morphology and crystal plane effect of Cu/CeO2 nanomaterial on the physicochemical and catalytic properties for carbonate hydrogenation, Catal. Sci. Technol. 6 (2016) 7752–7762.
[25] J. Ren, X. Liu, R.H. Gao, W.L. Dai, Morphology and crystal-plane effects of Zr-doped CeO2 nanocrystalson the epoxidation of styrene with tert-butylhydroperoxide as theoxidant, J. Energy Chem. 26 (2017) 681–687.
[26] L.J. Liu, Z.J. Yao, Y. Deng, F. Gao, B. Liu, L. Dong, Morphology and crystal-plane effects of nanoscale ceria on the activity of CuO/CeO2 for NO reduction by CO, Chem. Cat. Chem. 3 (2011) 978–989.
[27] H.X. Mai, L.D. Sun, Y.W. Zhang, R. Si, W. Feng, H.P. Zhang, H.C. Liu, C.H. Yan, Shape-selective synthesis and oxygen storage behavior of ceria nanopolyhedra, nanorods, and nanocubes, J. Phys. Chem. B 109 (2005) 24380–24385.
[28] D.C. Sayle, S.A. Maicaneanu, G.W. Watson, Atomistic models for CeO2(111), (110), and (100) nanoparticles, supported on yttrium-stabilized zirconia, J. Am. Chem. Soc. 124 (2002) 11429–11439.
[29] P. Li, Y. Zhou, Z.Y. Zhao, Q.F. Xu, X.Y. Wang, M. Xiao, Z.G. Zou, Hexahedron prism-anchored octahedronal CeO2: crystal facet-based homojunction promoting efficient solar fuel synthesis, J. Am. Chem. Soc. 137 (2015) 9547–9550.
[30] C. Guo, S.X. Wei, S.N. Zhou, T. Zhang, Z.J. Wang, S.P. Ng, X.Q. Lu, C.M.L. Wu, W. Y. Guo, Initial reduction of CO2 on Pd-, Ru-, and Cu-Doped CeO2(111) surfaces: effects of surface modification on catalytic activity and selectivity, ACS Appl. Mater. Interfaces 9 (2017) 26107–26117.
[31] W.X. Zou, B. Deng, X.X. Hu, Y.P. Zhou, Y. Pu, S.H. Yu, K.L. Ma, J.F. Sun, H.Q. Wan, L. Dong, Crystal-plane-dependent metal oxide-support interaction in CeO2/g-C3N4 for photocatalytic hydrogen evolution, Appl. Catal. B 238 (2018) 111–118.
[32] J. Bai, Y.Z. Sun, M.Y. Li, L. Yang, J. Li, The effect of phosphate modification on the photocatalytic H2O2 production ability of g-C3N4 catalyst prepared via acid-hydrothermal post-treatment, Diamond Relat. Mater 87 (2018) 1–9.
[33] W. Zhao, Z.Q. Yan, L. Qian, Graphitic carbon nitride: preparation, properties and applications in energy storage, Eng. Sci. 10 (2020) 24–34.
[34] C. Liu, Q.C. Fang, D.Y. Wang, C. Yan, F.Q. Liu, N. Wang, Z.H. Guo, Q.L. Jiang, Carbon and boron nitride nanotubes: structure, property and fabrication, ES Mater. Manuf. 3 (2019) 2–15, https://doi.org/10.30919/esmm5f199.
[35] P.T. Xie, Y. Liu, M. Feng, M. Niu, C.Z. Liu, N.N. Wu, K.Y. Sui, R.R. Patil, D. Pan, Z. H. Guo, R.H. Fan, Hierarchically porous Co/C nanocomposites for ultralight high-performance microwave absorption, Adv. Compos. Hybrid Mater. 2 (2021) 00202.
[36] H.K. Wu, Y. Zhang, R. Yin, W. Zhao, X.M. Li, L. Qian, Magnetic negative permittivity with dielectric resonance in random Fe3O4@graphene-phenolic resin composites, Adv. Comp. Hybrid Mater. 1 (2018) 168–176.
[37] N.N. Wu, X. Bai, D. Pan, B.B. Dong, R.B. Wei, N. Naik, R.R. Patil, Z.H. Guo, Recent advances of asymmetric supercapacitors, Adv. Mater. Interfaces 8 (2021), 2001710.
[38] Q.I. Xu, B.C. Zhu, B. Cheng, J.G. Yu, M.H. Zhou, Wk. Ho, Photocatalytic H2 evolution on graphdiyne/g-C3N4 hybrid nanocomposites, Appl. Catal. B 255 (2019), 117770.
[39] C.Z. Zhu, Y.T. Wang, Z.F. Jiang, F.C. Xu, Q.M. Xian, C. Sun, Q. Tong, W.X. Zou, X. G. Duan, S.B. Wang, CeO2 nanocrystal-modified layered MoS2/g-C3N4 as 0D/2D ternary composite for visible-light photocatalytic hydrogen evolution: interfacial consecutive multi-step electron transfer and enhanced H2O reactant adsorption, Appl. Catal. B 259 (2019), 118072.
[40] R. Hao, G. Wang, H. Tang, L. Sun, C. Xu, D. Han, Template-free preparation of macro/mesoporous g-C3N4/TiO2 heterojunction photocatalysts with enhanced visible light photocatalytic activity, Appl. Catal. B 187 (2016) 47–58.
[41] Q. Qiao, K. Yang, L.L. Ma, W.Q. Huang, B.X. Zhou, A.L. Pan, W.Y. Hu, X.X. Fan, G. F. Huang, Facile in situ construction of mediator-free direct Z-scheme g-C3N4/CeO2 heterojunctions with highly efficient photocatalytic activity, J. Phys. D Appl. Phys. 51 (2018), 275302.
[42] B. Hu, C.P. Cai, T.J. Chen, M.S. Fan, C.J. Song, X. Yan, W.D. Shi, Hydrothermal synthesis g-C3N4/nano-InVO4 nanocomposites and enhanced photocatalytic activity for hydrogen production under visible light irradiation, ACS Appl. Mater. Interfaces 7 (2015) 18247–18256.
[43] C.Z. Zhu, T. Gong, Q.M. Xian, J.M. Xie, Graphite-like carbon nitride coupled with tiny Bi2S3 nanoparticles as 2D/0D heterojunction with enhanced photocatalytic activity, Appl. Surf. Sci. 444 (2018) 75–86.
[44] M. Shi, S. Fujitsuka, T. Kim, Majima, Faster electron injection and more active sites for effcient photocatalytic H2 evolution in g-C3N4/MoS2 hybrid, Small 14 (2018), 1703277.
[45] S.Z. Hu, L. Ma, J.G. You, F.Y. Li, Z.P. Fan, G. Lu, D. Liu, J.Z. Gui, Enhanced visible light photocatalytic performance of g-C3N4 photocatalysts co-doped with iron and phosphorus, Appl. Surf. Sci. 311 (2014) 164–171.
[46] S. Kumar, M.B. Gawande, J. Kopp, S. Kment, R.S. Varma, R. Zboril, P- and F-co-doped carbon nitride nanocatalysts for photocatalytic CO2 reduction and thermocatalytic furanics synthesis from sugars, Chem. Sus. Chem. 13 (2020) 5231–5238.
[47] A. Viani, G. Mali, P. Macova, Investigation of amorphous and crystalline phosphates in magnesium phosphate ceramics with solid-state 1H and 31P NMR spectroscopy, Ceram. Int. 43 (2017) 6571–6579.
[48] P.Y. Kuang, B.C. Zhu, Y.L. Li, H.B. Liu, J.G. Yu, K. Fan, Graphdiyne: a superior carbon additive to boost the activity of water oxidation catalysts, Nanoscale Horiz. 3 (2018) 317–326.
[49] A.M. Puziy, O.I. Poddubnaya, A.M. Ziatdinov, On the chemical structure of phosphorus compounds in phosphoric acid-activated carbon, Appl. Surf. Sci. 252 (2006) 8036–8038.
[50] Y.J. Zhou, L.X. Zhang, J.J. Liu, X.Q. Fan, B.Z. Wang, M. Wang, W.C. Ren, J. Wang, M.L. Li, J.L. Shi, Brand new P-doped g-C3N4: enhanced photocatalytic activity for H2 evolution and Rhodamine B degradation under visible light, J. Mater. Chem. A 3 (2015) 3862.
[51] J.X. Low, C. Jiang, B. Cheng, S. Wageh, A.A. Al-Ghamdi, J.G. Yu, A review of direct Z-Scheme photocatalysts, Small Methods 1 (2017), 1700080.
[52] W.L. Shi, F. Guo, M.Y. Li, Y. Shi, M.J. Shi, C. Yan, Constructing 3D sub-micrometer CoO octahedrons packed with layered MoS2 shell for boosting photocatalytic overall water splitting activity, Appl. Surf. Sci. 473 (2019) 928–933.
[53] J.B. Diccianni, C. Hu, T. Diao, Insertion of CO2 mediated by a (Xantphos)NiI-Alkyl species, Angew. Chem. Int. Ed. 58 (2019) 13865–13868.